PAPER • OPEN ACCESS

# Mathematical modelling of haemorrhagic transformation within a multiscale microvasculature network

To cite this article: Jiayu Wang *et al* 2022 *Physiol. Meas.* **43** 055006

IOP Publishing Physiol. Meas. 43 (2022) 055006 https://doi.org/10.1088/1361-6579/ac6cc5

Physiological Measurement

IPEM Institute of Physics and Engineering in Medicine

OPEN ACCESS

RECEIVED
20 January 2022

REVISED
11 April 2022

ACCEPTED FOR PUBLICATION
4 May 2022

PUBLISHED
31 May 2022



PAPER

# Mathematical modelling of haemorrhagic transformation within a multiscale microvasculature network

**Jiayu Wang**[1], **Katinka R Van Kranendonk**[2], **Wahbi K El-Bouri**[3,4], **Charles B L M Majoie**[2] and **Stephen J Payne**[5]

[1] Institute of Biomedical Engineering, Department of Engineering Science, University of Oxford, Oxford, United Kingdom
[2] Department of Radiology and Nuclear Medicine, Amsterdam UMC, Location AMC, University of Amsterdam, Amsterdam, Netherlands
[3] Liverpool Centre for Cardiovascular Science, University of Liverpool and Liverpool Heart & Chest Hospital Liverpool, United Kingdom
[4] Department of Cardiovascular and Metabolic Medicine, University of Liverpool, United Kingdom
[5] Institute of Applied Mechanics, National Taiwan University, Taiwan

**E-mail:** Jiayu.wang@eng.ox.ac.uk

**Keywords:** haemorrhagic transformation, ischaemic stroke, microbleed, cerebral blood flow

## Abstract

*Objective.* Haemorrhagic transformation (HT) is one of the most common complications after ischaemic stroke, caused by damage to the blood–brain barrier (BBB) that could be the result of stroke progression or a complication of stroke treatment with reperfusion therapy. The aim of this study is to develop further a previous simple HT mathematical model into an enlarged multiscale microvasculature model in order to investigate the effects of HT on the surrounding tissue and vasculature. In addition, this study investigates the relationship between tissue displacement and vascular geometry. *Approach.* By modelling tissue displacement, capillary compression, hydraulic conductivity in tissue and vascular permeability, we establish a mathematical model to describe the change of intracranial pressure (ICP) surrounding the damaged vascular bed after HT onset, applied to a 3D multiscale microvasculature. The use of a voxel-scale model then enables us to compare our HT simulation with available clinical imaging data for perfusion and cerebral blood volume (*CBV*) in the multiscale microvasculature network. *Main results.* We showed that the haematoma diameter and the maximum tissue displacement are approximately proportional to the diameter of the breakdown vessel. Based on the voxel-scale model, we found that perfusion reduces by approximately 13–17% and *CBV* reduces by around 20–25% after HT onset due to the effect of capillary compression caused by increased interstitial pressure. The results are in good agreement with the limited experimental data. *Significance.* This model, by enabling us to bridge the gap between the microvascular scale and clinically measurable parameters, providing a foundation for more detailed validation and understanding of HT in patients.

## 1. Introduction

Stroke was ranked as the second leading cause of death across the world in 2010 (Lozano *et al* 2012, Iadecola *et al* 2020). With an increasingly elderly global population, the incidence of stroke is predicted to increase. Ischaemic stroke and haemorrhagic stroke are classified as the two main types of stroke based on their pathology. According to a study by Snarska *et al* (2016), the ratio of ischaemic stroke to haemorrhagic stroke is 4.8: 1. In the context of ischaemic stroke, however, it is also important to consider haemorrhagic transformation (HT), since this is a frequent, often asymptomatic, complication after acute ischaemic stroke onset (Álvarez-Sabín *et al* 2013), and one that can lead to long-term morbidity and mortality (Marsh *et al* 2013). Tan *et al* (2014) reported that spontaneous HT was observed in 50 of 407 patients (12.3%) and HT was observed in 29 patients (12%) in the study by Terruso *et al* (2009).

HT is usually classified according to the European Cooperative Acute Stroke Study II (ECASS II) classification based on radiological appearance (Milloy and Wood 2015). This classification divides HT into four types: haemorrhagic infarction type 1 (HI1), which is defined as small petechiae along the peripheral margins of

infarct; haemorrhagic infarction type 2 (HI2), defined as confluent petechiae within the infarcted area but without mass effect; parenchymal hematoma type 1 (PH1) as blood clots in $\leqslant$30% of the infarcted area with some slight mass effect; and parenchymal hematoma type 2 (PH2) as blood clots in $>$30% of the infarcted area with substantial mass effect (Milloy and Wood 2015).

HT is caused by disruption of the blood–brain barrier (BBB) and can result in significant damage to brain tissue. However, HT can also occur as a complication of stroke treatment with thrombolytic therapy (Group 1996) and often BBB breakdown can be caused by the combination of severe ischemic stroke and thrombolytic therapy (Lakhan *et al* 2013). The functional outcome of patients with HT varies, however patients with large hematomas are most likely to have a poor functional outcome (Van Kranendonk *et al* 2019).

A key question to answer is whether HT can be predicted accurately after ischaemic stroke, based on the available imaging data and other clinical parameters. Wang and Payne (2021) recently proposed a mathematical model that aimed to compare the severity of haemorrhage over a range of length scales and to investigate the effects of capillary compression on HT as the first step towards this objective. They established this simulation on a 2D vasculature model and assumed that the geometries of vessels in the same generation were the same. However, based on anatomical studies, capillaries have been shown to have a more web-like than tree-like structure. In addition, in the previous model, only one isolated vessel was assumed to be permeable and the effect of HT on neighbouring vessels was not considered.

It is thus necessary to extend this model to an enlarged vasculature length scale since it allows us to compare our model more accurately with the human vasculature. Various small-scale models (length scale order $\leqslant$100 $\mu$m) have been developed based on both human and rat cerebral vasculatures (Secomb *et al* 2000, Fang *et al* 2008, Su *et al* 2012, Safaeian and David 2013). However, these small models are limited by the difficulties of validation with clinical imaging, which is obtained at a voxel length scale (order 1 mm). In turn, large-scale models are mostly based on animal models (Gagnon *et al* 2015, Gould *et al* 2017, Schmid *et al* 2017). Many differences between animal and human vasculatures exist. For example, there are more penetrating venules than penetrating arterioles in the rat cortex, while human brains have the opposite ratio (Blinder *et al* 2010, Schmid *et al* 2019).

Human microvasculature models are still poorly understood due to the lack of physiological data and limited high-resolution imaging data. One blood flow model was generated by Lorthois *et al* (2011) based on human cerebral data (Cassot *et al* 2006) and it was shown that the simulation of blood flow highly depends on the prescribed boundary conditions of the vascular architecture. In addition, Linninger *et al* (2013) also used the same cerebral data to develop a large-scale vasculature model. In their simulation, the penetrating vessels were not generated by direct physiological data. El-Bouri and Payne (2018) thus subsequently developed a multiscale microvasculature model of the human cerebral cortex based on morphological data. They validated this model by calculating the cerebral blood flow (CBF) for voxels.

The aim of this study is to develop a model which is capable of simulating the severity of haemorrhage in penetrating networks. We use the mathematical model proposed by Wang and Payne (2021) as a starting point to simulate the haematoma formed from a single straight vessel. This mechanical model is then applied to the vasculature model generated by El-Bouri and Payne (2018). Properties such as cerebral blood volume ($CBV$) and perfusion rate are estimated and compared with clinical imaging data. Due to the increase in intracranial pressure (ICP) after HT, we also consider the effects of capillary compression in the vasculature, both in the damaged vessel and in other healthy vessels (Bordoni *et al* 2020). In addition, tissue displacement caused by the breakdown of BBB is calculated, using the methods proposed by Mokhtarudin and Payne (2015).

## 2. Materials and methods

The steps to simulate HT in our model are most conveniently split into two parts. In the first part, a simple model for one isolated penetrating vessel is considered as a starting point. This first part deals with the governing equations to investigate the mathematical modelling of both the penetrating vessels and the haematoma. The second part concerns the effects of the network haemodynamics, including the behaviour of $CBV$, perfusion and tissue displacement.

### 2.1. Model formulation

*2.1.1. Haemodynamics*

We begin with an isolated vessel, following the approach set out in Wang and Payne (2021). They simulated HT in a vascular model by assuming that blood vessels are completely permeable. In contrast, we assume that only the middle third of the vessel is permeable since the whole vessel is not thought to be leaky in HT, and this also avoids the edge effects at the connections with neighbouring vessels. Hence, we can also investigate the effect of capillary compression on the impermeable left third and right third due to increasing ICP, as shown in figure 1.

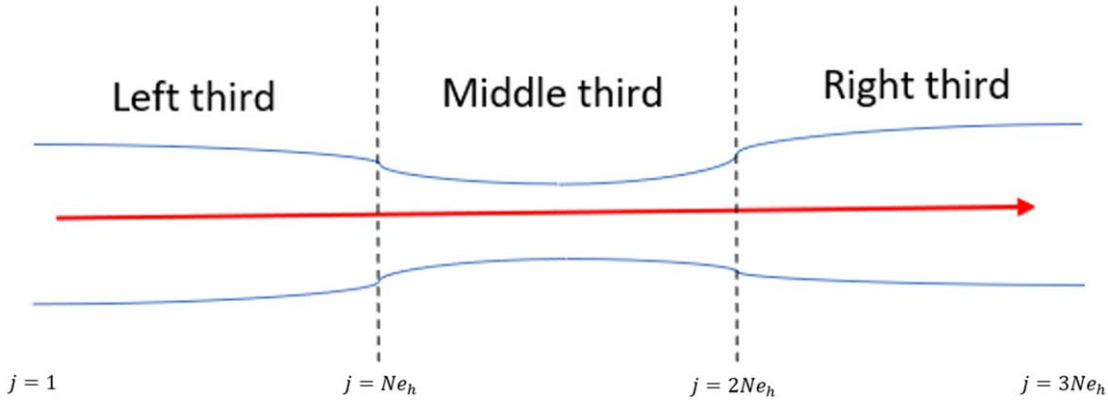


**Figure 1.** Schematic of single vessel model. The middle third of the vessel is assumed to be permeable with the remainder assumed impermeable. The resulting convexity of the capillary is due to the effects of capillary compression, as shown previously (Wang and Payne 2021). Red arrow denotes direction of blood flow.

The vessel is divided into $3 \times Ne_h$ cylindrical elements, where $j = 1,\ldots,Ne_h,\ldots,2Ne_h,\ldots,3Ne_h$. In addition, the surrounding tissue is divided into $Ne_v$ elements along its axial direction, where $i = 1,\ldots,Ne_v$. Pozrikidis and Farrow (2003) selected 96 elements for a capillary vessel. Thus, in this simulation, $Ne_h = Ne_v = 100$ is set to obtain a good balance between computational expense and model accuracy: we find that this keeps the impact of adjustment of the node coordinate points in the penetrating network to fit the grid intersection to less than 1% (this adjustment will be discussed later in this section). In this simulation, we model the HT in arterioles with different diameters, from 15 $\mu$m to 250 $\mu$m but with the same length, to quantify haematoma volume and tissue displacement. The depth of the cerebral cortex is suggested to be approximately 2.5 mm (Duvernoy *et al* 1981). Thus, a typical penetrating vessel length is chosen to be 1.25 mm in this simulation.

Wang and Payne (2021) established a series of governing equations to calculate blood flow rate $Q$, capillary pressure $p_c$ and tissue pressure distribution $p_i$ (equation (1)) for HT in an isolated permeable vessel and identified the haematoma boundary through setting a pressure boundary condition:

$$p_i(\mathbf{x}) = P_o + \frac{D}{4}\int_s p_{io}(\mathbf{x}')\frac{|\mathbf{R} - \mathbf{R}'|}{(|\mathbf{Z} - \mathbf{Z}'|^2 + |\mathbf{R} - \mathbf{R}'|^2)^{\frac{3}{2}}}\mathrm{d}Z' \tag{1}$$

where $P_o$ denotes the far-field interstitial pressure, $D$ denotes the diameter of the vessel, $S$ denotes the surface area of the vessel, $p_{io}$ denotes the exterior interstitial pressure, point $\boldsymbol{x}$ in tissue can be defined as $\boldsymbol{x} = (Z,\ R,\ \theta)$ and thus, $\boldsymbol{x}' = (Z',\ R',\ \theta')$, where the $Z$-axis is the direction along the capillary, the $R$-axis is the radial direction and $\theta$ is the angle of rotation. The origin of the coordinate system is set at the inlet centre point of the vessel. In addition, the definition of the haematoma boundary used here is based on that proposed by Wang and Payne (2021): thus, we used a value set at 0.1 mmHg above $P_o$ ($P_o = 15$ mmHg). This definition of haematoma is chosen as it gives results that seem to be the closest to the experimental data measured by Jenkins *et al* (1989) in that the distance in mice between the edge of a haematoma and related damaged vessels is approximately 700 $\mu$m.

*2.1.2. Capillary compression*

Wang and Payne (2021) discussed the effects of capillary compression based on experimental data (Bordoni *et al* 2020). However, this approach is less suitable for determining the capillary compression for large arterioles ($D > 25$ $\mu$m). Arteriolar diameters are typically found in the range $15 - 240$ $\mu$m and venule diameters in the range $20 - 125$ $\mu$m (Duvernoy *et al* 1981). Thus, the more general relationship between pressure and cross-sectional area of the capillary (collapse equation) developed by Drzewiecki *et al* (1997) is used here to simulate vessel compression:

$$\Delta P = -\frac{E{h_b}^3}{9{r_{mb}}^3}\left[\left(\frac{A_b}{A}\right)^n - 1\right] \tag{2}$$

where $\Delta P = p_c - p_{io}$ denotes transmural pressure, $E$ denotes wall elastic modulus, $h_b$ denotes vascular wall thickness at maximum compliance point, $r_{mb}$ denotes the vessel lumen radius at its maximum compliance point, $A_b$ denotes the vessel lumen cross-sectional area at its maximum compliance point, $A$ denotes vascular lumen cross-sectional area and $n$ denotes the constant that defines the degree of curvature of the pressure-area relationship. In this simulation, we have selected measurements from the canine carotid artery and jugular vein to determine the compression model for arterioles and venules in penetrating networks, as shown in table 1.

**Table 1.** Vascular measured characteristics.

| Vascular type | E | $h_b$ | n |
|---|---|---|---|
| Canine carotid artery (Drzewiecki *et al* 1997) | 29.2 mmHg | 0.787 mm | 3.380 |
| Canine jugular vein (Drzewiecki *et al* 1997) | 9530.0 mmHg | 0.401 mm | 0.137 |

**Table 2.** List of parameters and their baseline value for the proposed model.

| Parameter | Model values | Reference |
|---|---|---|
| Biot parameter for water network, $\alpha^w$ | 1 | Tully and Ventikos (2011) |
| Shear modulus, G | 216.3 Pa | Mokhtarudin and Payne (2015) |
| Poisson's ratio, v | 0.35 | Drake *et al* (1996) |

*2.1.3. Tissue displacement*

To determine the tissue displacement after HT onset, the equations developed by Mokhtarudin and Payne (2015) were used, assuming quasi steady state based on the fact that the tissue displacement process occurs slowly with negligible inertial effects (Terzaghi 1943):

$$\nabla^2 U - \omega \nabla p_i = 0 \tag{3}$$

$$\omega = \alpha^w / \left( G + \frac{G}{1 - 2\nu} \right) \tag{4}$$

where $U$ denotes tissue displacement, $\alpha^w$ denotes the Biot parameter for water, $G$ is the shear modulus and $\nu$ is Poisson's ratio. $\omega$ can thus be calculated to be 0.001 $Pa^{-1}$. The values used here are given in table 2.

## 2.2. Network model

The penetrating network model used in this simulation is directly taken from El-Bouri and Payne (2018). They used a statistically representative large-scale model ($1 \times 1 \times 2.5$ mm) to investigate the effects of a penetrating vessel occlusion on blood flow and blood pressure in the human cortex. To extend this model, we repeat a $1 \times 1 \times 2.5$ mm voxel four times to give a final volume of $2 \times 2 \times 2.5$ mm in order to fully present the appearance of the haematoma in the network (this is required since the maximum haematoma radius obtained by Wang and Payne (2021) is larger than 500 $\mu$m), as shown in figure 2.

The penetrating vessels descend into the cerebral cortex from the pial surface. Arteriolar pial pressure is assumed to be 90 mmHg and venule pial pressure is set to be 25 mmHg, since arteriole pial pressure is in the range $65 - 90$ mmHg and venule pial pressure in the range 15 to 25 mmHg (Stromberg and Fox 1972, Tamaki and Heistad 1986). We thus choose 90 mmHg and 25 mmHg here to show a relatively severe scenario. The total pressure drop for arterioles is assumed to be 35 mmHg, and for venules, the total pressure drop is assumed to be 15 mmHg (Zweifach and Lipowsky 1977). In each $1 \times 1 \times 2.5$ mm voxel, it is assumed that there are 12 starting points of penetrating vessels in the ratio 2:1 arterioles-to-venules, all randomly distributed across the surface.

In this simulation, the height of the $2 \times 2 \times 2.5$ mm voxel is divided into $6 \times Ne_h$ elements since the height of the voxel is double the length of the single vessel simulated previously. Taking the central axis of the cuboid as the centre, the $\sqrt{2}$ mm radius (diagonal length in figure 2(b)) is divided into $Ne_v$ elements. Each node in the vasculature is adjusted slightly to fit the grid intersection. For example, node I (solid black circle) in figure 2(b) is adjusted to the dashed black circle above. The impact of this adjustment can be neglected, since the results of $CBV$ and perfusion rate are both found to change by less than 1% based on our simulations (results not shown).

It is then assumed that HT occurs in the penetrating arteriole in the centre of the $2 \times 2 \times 2.5$ mm voxel. This is based on the results of Thevathasan *et al* (2018) who have shown that the cortical involvement rate is 93% for HT patients, i.e., that the rate that HT occurs in the penetrating network is high, leading us to assume that the HT occurs in the largest vessel in our model. The middle third of this vessel is set to be permeable with the remainder impermeable, to be consistent with the previous model. In this simulation, the diameter of arterioles and venules are set to be $40 \pm 8$ $\mu$m and $110 \pm 16$ $\mu$m respectively. Ten geometrically representative voxels were used to calculate the changes in perfusion rate and $CBV$ in response to HT. These two parameters were

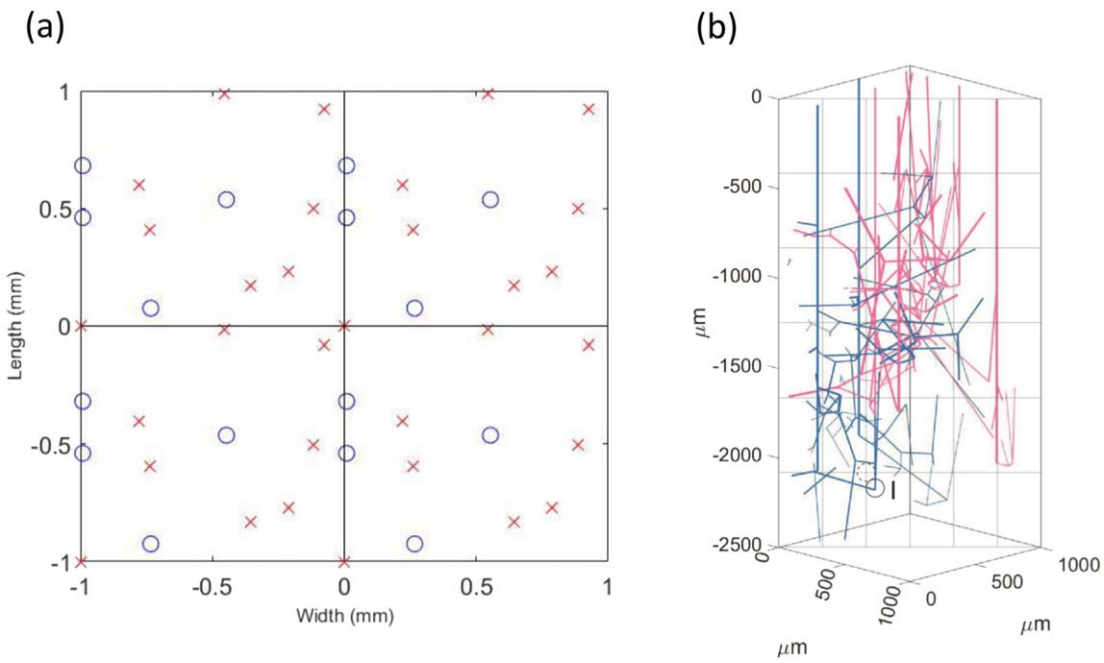


**Figure 2.** (a) Top-down view of a 2 × 2 × 2.5 mm voxel, split into four quadrants each containing eight arterioles and four venules. Red crosses represent arterioles and blue circles represent venules. (b) A fourth example voxel show half the penetrating vessels for easier viewing. The penetrating vessels enter from the pial surface into the grey matter. The diagonal length of the horizontal plane is $\sqrt{2}$ mm.

selected as they can be measured at a voxel length scale using a number of imaging modalities, such as computed tomography perfusion (CTP).

The perfusion rate, $F$ can be calculated by using the pressure drop and total resistance:

$$F = \frac{Q \times 60 \times 100}{V \times \rho} \tag{5}$$

where $Q$ denotes the blood flow rate, calculated by summing the blood flow leaving the voxel (El-Bouri and Payne 2016), $V$ denotes the volume of tissue, $\rho$ is cerebral tissue density (0.96 gcm$^{-3}$) (Dekaban and Sadowsky 1978, Lüders *et al* 2002), and factors of 60 and 100 are used in the equation to convert seconds to minutes and g to 100 g, respectively. Based on equation (2), the vascular diameter distribution $D^j$ in each voxel can be determined. Then the $CBV$ can be calculated:

$$CBV = \sum (D^j/2)^2 L \times \frac{6Ne_h}{V \times \rho} \tag{6}$$

where $L$ denotes each vascular length in the voxel and $j = 1,\ldots,6Ne_h$. In this simulation, haematoma is assumed to be of the form with no mass effect. The changes in $CBV$ and $F$ are due to capillary compression caused by increased ICP.

## 3. Results

### 3.1. Single vessel model

Using equation (1), the tissue pressure distribution $p_i$ can be calculated for each vessel with diameters ranging from 15 $\mu$m to 250 $\mu$m. By applying the proposed definition of the haematoma boundary, i.e., 15.1 mmHg, we can determine the haematoma radius and volume for each simulation. Haematoma radius and volume were found to increase rapidly with vessel diameter, as shown in figures 3(a) and (c). When the vessel diameter is set to 15 $\mu$m, the maximum haematoma radius is 290.7 $\mu$m. The maximum haematoma radius for a 250 $\mu$m diameter vessel is calculated to be 5.1 mm. Figure 3(b) shows, however, that the ratio of haematoma radius to vascular diameter is nearly constant for different diameter vessels: the ratio is approximately 20 over the leaky part of the vessel.

In this simulation, the haematoma volume is found to be 0.097 mm$^3$ when the arteriole diameter is set to 15 $\mu$m and is calculated to be 62.3 mm$^3$ for 250 $\mu$m arteriole diameter, showing a very wide range of values and a very strong sensitivity to the vessel diameter. The characteristic length of the haematoma is shown in figure 3(d): characteristic length increases sharply between the small and large vessels, diameter $<25$ $\mu$m (slope

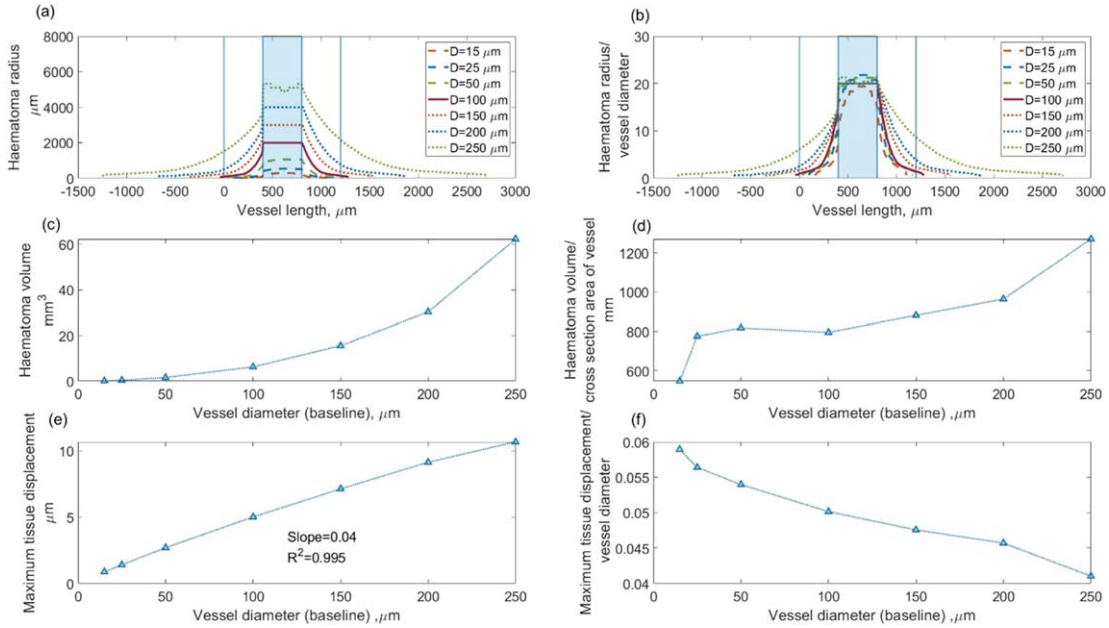


**Figure 3.** (a) Haematoma radius variation with axial length. The isolated vessel starts from 0 $\mu$m to 1200 $\mu$m and permeable section from 400 $\mu$m to 800 $\mu$m. (b) The ratio of haematoma radius to vessel diameter varies with axial length. (c) Haematoma volume variation with vessel diameter. (d) Characteristic length variation with vessel diameter. (e) Variations in maximum tissue displacement in vessel diameter. (f) Ratio of maximum tissue displacement to vessel diameter behaviour with variable vessel diameter.

=22780) and >200 $\mu$m (slope =6100) but remains approximately constant over the diameter range 25 $\mu$m to 150 $\mu$m, as shown in figure 3(d).

As shown in figure 3(e), larger arteriolar diameter leads to larger maximum tissue displacement, as would be expected. In this simulation, the maximum tissue displacement for each vessel is in the order of $10^0$ $\mu$m. The slope of the maximum tissue displacement and vessel diameter is close to 0.04 ($R^2 = 0.995$). Combinations of vector and contour plots of tissue displacement are also shown in figures 4(b), (e) and (h) to show the distribution of tissue displacement for different arteriolar diameters. Tissue displacement, as expected, is found to point from high pressure positions to low pressure positions. Note that tissue displacement is a vector that follows the same direction as the pressure field. It can be seen, therefore, that the tissue displacement is not perfectly radial to the vessel surface at the junction of the leaky part and nonleaky part, hence showing the need for a full 3D simulation. Dimensionless tissue displacement for the 15 $\mu$m diameter vessel is also shown in figure 5.

Figures 4(a), (d) and (g) show comparisons of variable vascular diameter along the axial length based on equation (2) for three different sized vessels. Larger vessels are compressed more due to larger exterior interstitial pressure (Wang and Payne 2021). In addition, the vessel sections before and after the junctions of the leaky and nonleaky parts are also found to be compressed. The tissue pressure distributions are shown in figures 4(c), (f) and (i) for different vessel diameters: 15 $\mu$m, 100 $\mu$m and 250 $\mu$m, respectively. Larger leaky vessels lead to higher tissue pressure surrounding the vessel: presssure scale varies from 15–21 mmHg, 15–49 mmHg and 15–76 mmHg for different vessel diameters: 15 $\mu$m, 100 $\mu$m and 250 $\mu$m, respectively.

### 3.2. Network model

We next simulate HT in the voxel containing 32 arterioles and 16 venules, an example of which is shown in figure 6. Ten simulations based on statistically accurate voxels of the penetrating vessels were run to determine the growth of HT. This 2 × 2 × 2.5 mm voxel is found fully to contain the haematoma. In this voxel, the middle third of the central vessel is assumed to be permeable and this is the case for all simulations across the different vasculature networks in the different voxels.

In these simulations, we find that the ranges of $CBV$ before HT and after HT in these voxels are 15–32 ml/100 g and 11–23 ml/100 g, respectively. As shown in figure 7(b), $CBV$ reduces by around 20–25% after HT onset. Perfusion rate is calculated by summing the flow leaving the terminal arterioles within the voxel boundary. Figure 7(b) shows that perfusion reduces by approximately 13–17% after HT onset in the voxel, which is a smaller change than that exhibited by $CBV$.

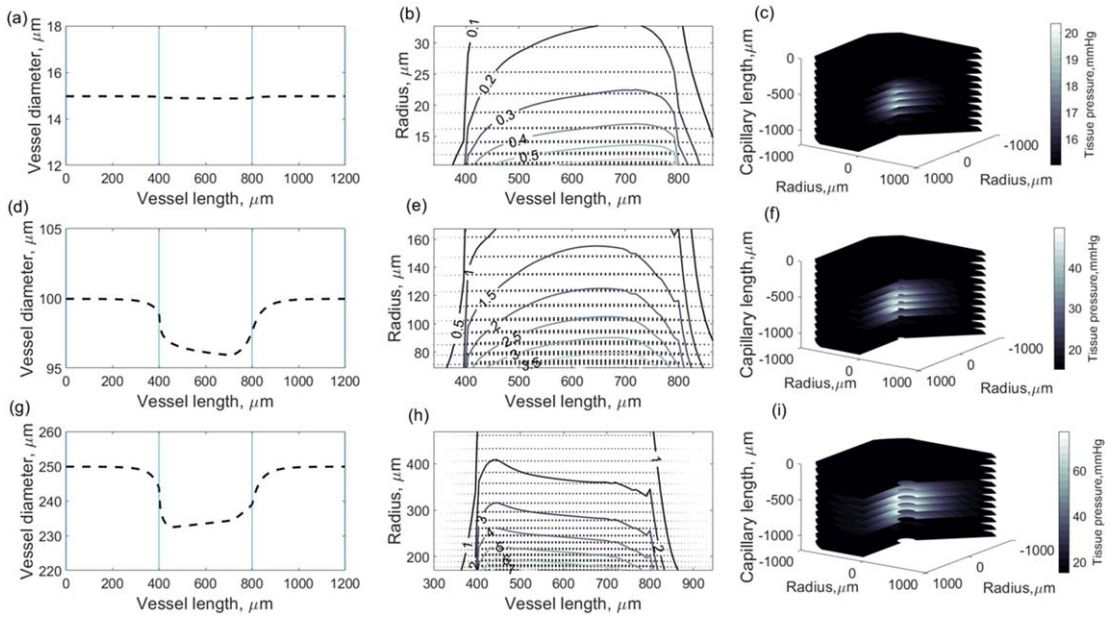


**Figure 4.** (a), (d) and (g): Vessel diameter variation with axial length, baseline diameter = 15 $\mu$m, 100 $\mu$m and 250 $\mu$m, respectively. (b), (e) and (h): Combinations of vector and contour plots of tissue displacement, baseline diameter = 15 $\mu$m, 100 $\mu$m and 250 $\mu$m, respectively. $y$-axis represents the radial direction. The units for these contour plots are $\mu$m. (c), (f) and (i): Slices of the pressure map, baseline diameter = 15 $\mu$m, 100 $\mu$m and 250 $\mu$m, respectively. Note that the pressure axis is different in each simulation for ease of viewing.

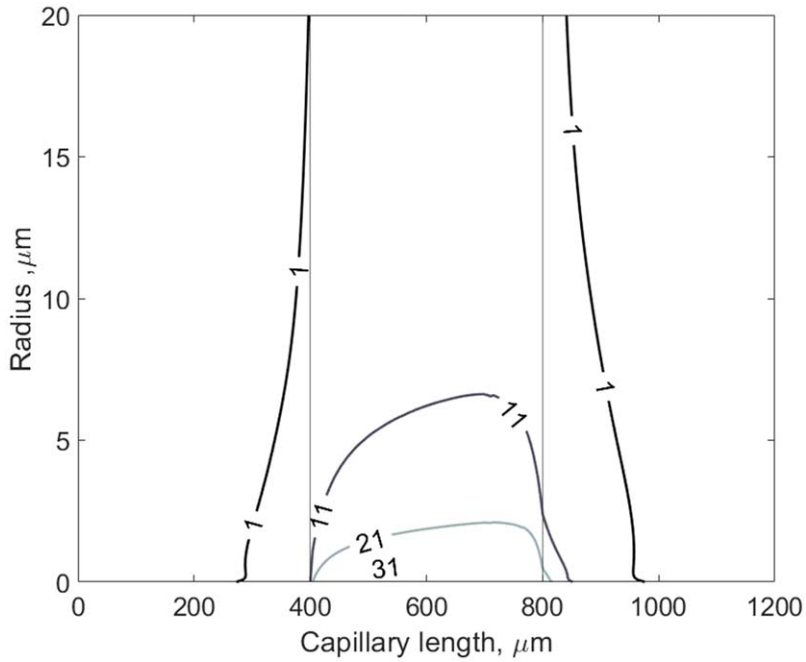


**Figure 5.** Contour plot of dimensionless tissue displacement. Values are given in percent.

## 4. Discussion

We have developed here a HT model in a microvasculature network model to investigate how cerebral haemodynamics can be affected after HT onset. This simulation is based on the model proposed by Wang and Payne (2021) that presents a mathematical model of HT after ischaemic stroke. They focused on how changes in vascular geometry can affect the severity of HT, thus they assumed that the whole vessel was permeable. To develop further these simulations, in the first part of this model we assumed that only the middle third of the vessel is permeable to determine the effect of HT on the remaining healthy vasculature. We determine that the

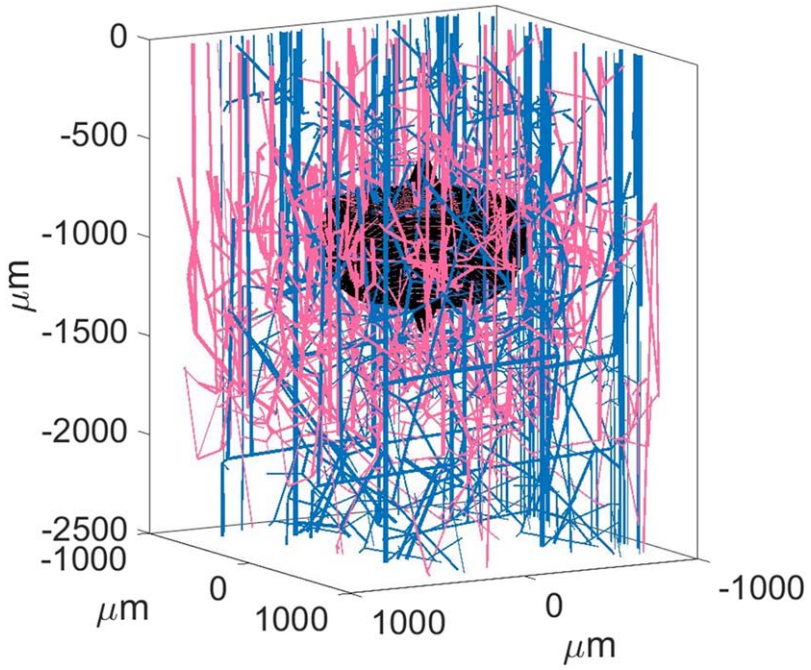


**Figure 6.** Example voxel showing a haematoma located in the middle third of the central penetrating arteriole. Red vessels represent arterioles and blue vessels denote venules. The penetrating vessels enter from the top pial surface into the grey matter, coupling to the capillary bed continuum via the terminal vessels.

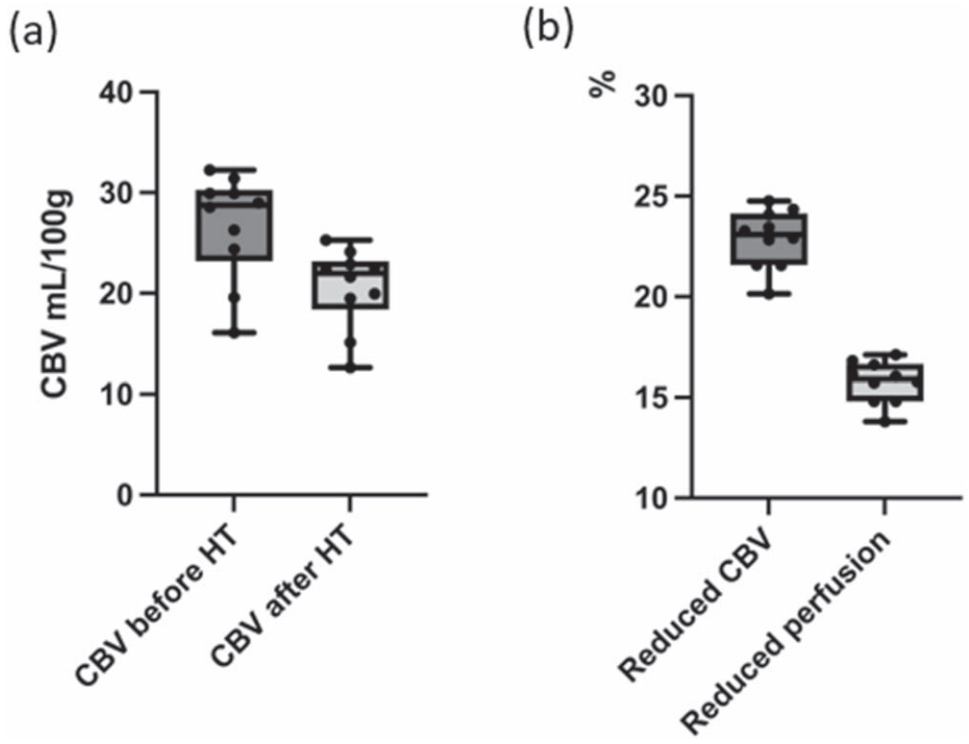


**Figure 7.** (a) Comparison of *CBV* before and after HT in voxel. (b) The percentage change of *CBV* and perfusion after HT.

haematoma diameter and the maximum tissue displacement are approximately proportional to the diameter of the breakdown vessel. Then in the second part of this simulation, we quantified changes in haemodynamics after HT onset in the 3D microvasculature, as these directly relate to parameters that can be measured at this voxel length scale. Based on the voxel-scale model, we determine that the prefusion reduces by approximately 13–17% and *CBV* reduces by around 20–25% after HT onset in a single penetrating vessel.

In the simulation for the single vessel, the left third and the right third of the vessel are both surrounded by the haematoma, i.e., blood diffuses to the tissue around healthy parts of blood vessels following the direction of high pressure to low pressure. Vessels with a larger diameter result in a larger haematoma radius and hence a longer diffusion path than smaller vessels, which also indicates that the high tissue pressure field volume is larger in larger leaky vessels than in smaller vessels. A larger high tissue pressure field volume seems to aggregate more blood and to cause a severe space-occupying effect. These results are similar to the results shown by Wang and Payne (2021), who concluded that the arterioles cause a larger haematoma radius and a larger leakage flowrate compared to capillaries. This result might help to explain the variable behaviour of HT, i.e., why some patients have HI1/HI2 and why other patients have PH1/PH2, dependent upon the type of leaky vessel. More work will be required to explore this effect and to link the model predictions with clinical imaging, however, following on from the classification proposed by von Kummer *et al* (2015).

To the best of our knowledge, there are limited available experimental data that describe the development of a haematoma for an individual capillary after HT onset. Jenkins *et al* (1989) measured the distance between the haematoma boundary and related damaged vessels as 700 $\mu$m in mice, which is well within this simulation's range of haematoma radius. We also find here that the ratio of haematoma radius to vascular diameter is approximately constant for the leaky part over a wide range of vessel radius, as shown in figure 3(b). However, the ratio is found to be larger for the tissue around the impermeable part of larger vessels than for smaller vessels.

We have improved the methods to investigate the capillary compression in this simulation compared with the model developed by Wang and Payne (2021), who used the experimental data by Bordoni *et al* (2020). In their experiment, they set the cerebral perfusion pressure (capillary pressure in our case) to be 38.4 mmHg. Nevertheless, in our simulation, we set the capillary pressure to vary along the vessel and the inlet capillary pressure (arteriole pial pressure) to be 90 mmHg. In addition, Wang and Payne (2021) found that based on these experimental data, larger vessels (diameter $>23.97$ $\mu$m) with higher blood flow rates have a higher leakage rate of blood and higher exterior interstitial pressure than smaller vessels, such that this situation may result in larger vessels becoming fully constricted. Even a mild constriction is able to cause a large effect on flow, due to the strong nonlinearity in the viscosity-diameter relationship (Pries and Secomb 2005).

Hence, we use here the transmural pressure and cross section area relationship for collapsible blood vessels, proposed by Drzewiecki *et al* (1997), in this simulation. However, this method still contains limitations: in particular, the proposed model has yet to consider an autoregulation mechanism for variations in perfusion rate and interstitial pressure. To the best of our knowledge, the mechanism of autoregulation in HT remains very poorly understood or quantified, and there is no model yet of how autoregulation behaves at this length scale, making it difficult to incorporate within our model (Strandgaard *et al* 1973, Nakagawa *et al* 2011). In particular, the balance between autoregulation in the arteriolar network and the capillary bed remains controversial and much more detailed experimental data will be required to understand better the response at an individual vessel scale. However, once more is known about the behaviour of autoregulation at this length scale, it will be possible to incorporate this within our model relatively straightforwardly.

The order of magnitude of maximum tissue displacement is about 1–10 $\mu$m and the maximum dimensionless tissue displacement is approximately 30%. However, the experimental data of tissue displacement in HT are extremely limited. Mokhtarudin and Payne (2015) proposed that the maximum tissue displacement under condition of ischemia–reperfusion varies from 0.97 to 7.21 mm and that the dimensionless tissue displacement is approximately in the range of 0–25%, values which are in very good agreement with the those that we obtain here.

As shown in figure 7(b), a reduction in $CBV$ is found following HT, in the range of 20–25% and the perfusion also reduces by approximately 13–17% after HT onset. Jain *et al* (2013) compared the CT perfusion parameters for a control group and a HT group: the mean reduction rate of $CBV$ is $19 \pm 6.8$% and the mean reduction rate of relative cerebral blood flow (rCBF) (reduction rate of perfusion in our case) is $10 \pm 4.3$%, both of which are in reasonably good agreement with the results that we present here. Seki *et al* (1985) proposed that a reduction in $CBF$ to 50% of normal could be considered as a critical value for HT development. Thereafter, they found CBF decreased rapidly. This indicates that in the next stages of model development, it will be important to include the time dynamics in the HT simulation.

In this study, our results are found to be within the range of CBV and perfusion values found from experiments but lie within the top half of this range. We suggest that this is the case because we set the arterioles to be leaky in this study, which can cause more severe HT since the blood pressure here is higher compared to the capillary and venous circulations. rCBF is calculated clinically from data collected on the ipsilateral side compared with the contralateral (healthy) side. Our perfusion change is calculated by the change in perfusion after HT onset compared with the healthy state. Perfusion and rCBF can therefore be assumed to directly equivalent in this case.

When haemorrhage occurs in a patient's brain, multiple vessels probably leak simultaneously and the leaky regions along the vessels are not certain. In this simulation, we set the middle third of the vessel to be permeable

and the remainder to be healthy to develop further the model proposed by Wang and Payne (2021), where it was assumed that the whole vessel was leaky. It is straightforward to relax this assumption, but the main aim of this study is to determine how HT in a single vessel can affect the surrounding vessels and tissue. Pozrikidis and Farrow (2003) also used the same approach (the middle third of vessel being permeable) in their tumour simulations, which makes it easier to compare our results with those of Pozrikidis. We also choose the middle third to avoid edge effects at the nodes between blood vessels. In addition, the haemorrhage caused by one microvascular vessel can be affected by the surrounding circulation. However, the tissue surrounding the penetrating network is assumed to be homogeneous. The haemorrhage model applied in different regions should be adjusted due to the spatially varying mechanical parameters of the tissue.

In our simulation, the formation of haematoma is assumed to be fast enough such that haemostasis does not occur. Wang and Payne (2021) calculated that the time to haematoma formation is in the order of ten times faster than haemostasis. However, haemostasis should certainly be considered in the following stages of model development due to localized vasoconstriction occurring before haemostasis starts (Armstrong and Golan 2011). Localized vasoconstriction caused by haemostasis could be another source of the compression of vessels since we only consider capillary compression due to increasing ICP.

By transforming our earlier 2D model to a 3D model in this study, the HT damage to the surrounding tissue and healthy vessels can now be estimated. It can be seen that the geometry of the 3D network is highly complex and that it would not be straightforward to derive an equivalence between this model and the earlier 2D model, although we note that with adequate and detailed clinical data, the 2D model could allow clinicians to model the consequences of HT. Meanwhile, in future research, we will apply this HT model in a full-brain 3D model in order to validate with clinical imaging data, since although the CT image is 2D, clinicians calculate the haematoma volume by overlapping the slices of CT images to create a 3D brain map.

Regarding the identifiability aspects of the model, nearly all the parameters that we are using here are likely to vary from one patient to another (to a greater or lesser degree). However, we suspect that vascular permeability is the most likely to vary most significantly from one patient to another and, based on our results, this means that this parameter would seem to be the most readily identifiable. However, this remains to be confirmed in our future work. It should be noted that the values of CBV and perfusion given here do not match directly to a specific dataset.

The aim of our work is thus to identify those patients who are most at risk of haemorrhage based on imaging data (and other nonimaging parameters). In the previous study, Wang and Payne (2021) proposed a mathematical model to simulate HT and extended this model to a penetrating network in this study. They have investigated how the different geometry and haemodynamics affect the consequences of haemorrhage. By using cerebral angiography, clinicians are able to predict the locations of potential vulnerable vessels and severity of HT, in order to assist them in selecting which patients who are not suitable for rt-PA treatment.

It will therefore be necessary to extend our model to an enlarged vasculature length scale and to apply it in other regions in the brain. In addition, in the next stage of the model development, more leaky random vessels should be introduced. Van Kranendonk *et al* (2020) measured median haemorrhage volume to be 3.37 ml based on imaging data, which is in the order of magnitude of $10^2$ times larger than our one leaky vessel. This higher value of haematoma volume is to be expected, due to multiple vessels likely being leaky in HT. Thus, in real scenarios, a first estimate would be that approximately 100 vessels exhibit leakage, which is a relatively large number. Thus, it will be necessary to simulate multiple permeable vessels in the vasculature and to investigate the interaction of these vessels with the surrounding vessels. This will be the subject of a future study. Meanwhile, by using a full brain model, clinicians can stratify vulnerable patients more accurately using CT imaging data. The risk and consequences of HT caused by the different locations of stroke can thus be identified.

## 5. Conclusions

Through the development of a mathematical model to simulate HT within a multiscale microvasculature network, it is possible to simulate the severity of HT and haemodynamics after HT onset. This study has identified that the haematoma radius is approximately proportional to the diameter of the vessel. This model indicates that larger vessel breakdown leads to larger haematoma radius, higher tissue displacement and higher ICP. These results may be able to explain the different categories of HT that have been found clinically. One of the more significant highlights is that we are able to compare this simulation of HT based on the reductions in both cerebral blood volume and perfusion. We determine a reduction in CBV in the range of 20–25% and in perfusion of approximately 13–17% after HT onset. The solutions and insights gained from this study may be of assistance in future to assess the impact of HT on an enlarged 3D tissue region and at a whole-brain scale.

## ORCID iDs

Stephen J Payne https://orcid.org/0000-0003-1156-2810

## References

Álvarez-Sabín J, Maisterra O, Santamarina E and Kase C S 2013 Factors influencing haemorrhagic transformation in ischaemic stroke *Lancet Neurol.* **12** 689–705

Armstrong A W and Golan D E 2011 Pharmacology of hemostasis and thrombosis *Principles of Pharmacology: The Pathophysiologic Basis of Drug Therapy* 3rd edn (Philadelphia: Lippincott Williams & Wilkins) 372–400

Blinder P, Shih A Y, Rafie C and Kleinfeld D 2010 Topological basis for the robust distribution of blood to rodent neocortex *Proc. Natl Acad. Sci.* **107** 12670–5

Bordoni L, Li B, Kura S, Boas D A, Sakadžić S, Østergaard L, Frische S and Gutiérrez-Jiménez E 2020 Quantification of capillary perfusion in an animal model of acute intracranial hypertension *J. Neurotrauma* **38** 446–54

Cassot F, Lauwers F, Fouard C, Prohaska S and Lauwers-Cances V 2006 A novel three-dimensional computer-assisted method for a quantitative study of microvascular networks of the human cerebral cortex *Microcirculation* **13** 1–18

Dekaban A S and Sadowsky D 1978 Changes in brain weights during the span of human life: relation of brain weights to body heights and body weights *Ann. Neurol.* **4** 345–56

Drake J, Mostachfi O, Tenti G and Sivaloganathan S 1996 Realistic simple mathematical model of brain biomechanics for computer simulation of hydrocephalus and other brain abnormalities *Can. J. Neurol. Sci* **23** 345–56

Drzewiecki G, Field S, Moubarak I and Li J K-J 1997 Vessel growth and collapsible pressure-area relationship *Am. J. Physiol. Heart. Circ. Physiol.* **273** H2030–43

Duvernoy H M, Delon S and Vannson J 1981 Cortical blood vessels of the human brain *Brain Res. Bull.* **7** 519–79

El-Bouri W K and Payne S J 2018 Investigating the effects of a penetrating vessel occlusion with a multi-scale microvasculature model of the human cerebral cortex *NeuroImage* **172** 94–106

El-Bouri W K and Payne S J 2016 A statistical model of the penetrating arterioles and venules in the human cerebral cortex *Microcirculation* **23** 580–90

Fang Q, Sakadžić S, Ruvinskaya L, Devor A, Dale A M and Boas D A 2008 Oxygen advection and diffusion in a three-dimensional vascular anatomical network *Opt. Express* **16** 17530–41

Gagnon L, Sakadžić S, Lesage F, Musacchia J J, Lefebvre J, Fang Q, Yücel M A, Evans K C, Mandeville E T and Cohen-Adad J 2015 Quantifying the microvascular origin of BOLD-fMRI from first principles with two-photon microscopy and an oxygen-sensitive nanoprobe *J. Neurosci.* **35** 3663–75

Gould I G, Tsai P, Kleinfeld D and Linninger A 2017 The capillary bed offers the largest hemodynamic resistance to the cortical blood supply *J. Cereb. Blood Flow Metab.* **37** 52–68

Group M A S T E S 1996 Thrombolytic therapy with streptokinase in acute ischemic stroke *New Engl. J. Med.* **335** 145–50

Iadecola C, Buckwalter M S and Anrather J 2020 Immune responses to stroke: mechanisms, modulation, and therapeutic potential *J. Clin. Investig.* **130** 2777–88

Jain A, Jain M, Kanthala A, Damania D, Stead L, Wang H and Jahromi B 2013 Association of CT perfusion parameters with hemorrhagic transformation in acute ischemic stroke *Am. J. Neuroradiol.* **34** 1895–900

Jenkins A, Maxwell W and Graham D 1989 Experimental intracerebral haematoma in the rat: sequential light microscopical changes *Neuropathol. Appl. Neurobiol.* **15** 477–86

Lakhan S E, Kirchgessner A, Tepper D and Aidan L 2013 Matrix metalloproteinases and blood-brain barrier disruption in acute ischemic stroke *Frontiers Neurol.* **4** 32

Linninger A, Gould I, Marinnan T, Hsu C-Y, Chojecki M and Alaraj A 2013 Cerebral microcirculation and oxygen tension in the human secondary cortex *Ann. Biomed. Eng.* **41** 2264–84

Lorthois S, Cassot F and Lauwers F 2011 Simulation study of brain blood flow regulation by intra-cortical arterioles in an anatomically accurate large human vascular network. Part II: flow variations induced by global or localized modifications of arteriolar diameters *Neuroimage* **54** 2840–53

Lozano R, naghavi M, Foreman K, Lim S, Shibuya K, Aboyans V, Abraham J, Adair T, Aggarwal R and Ahn S Y 2012 Global and regional mortality from 235 causes of death for 20 age groups in 1990 and 2010: a systematic analysis for the global burden of disease study 2010 *Lancet* **380** 2095–128

Lüders E, Steinmetz H and Jäncke L 2002 Brain size and grey matter volume in the healthy human brain *Neuroreport* **13** 2371–4

Marsh E B, Llinas R H, Hillis A E and Gottesman R F 2013 Hemorrhagic transformation in patients with acute ischaemic stroke and an indication for anticoagulation *Eur. J. Neurol.* **20** 962–7

Milloy M and Wood E 2015 Withdrawal from methadone in US prisons: cruel and unusual? *Lancet* **386** 316–8

Mokhtarudin M M and Payne S 2015 Mathematical model of the effect of ischemia–reperfusion on brain capillary collapse and tissue swelling *Math. Biosci.* **263** 111–20

Nakagawa K, Serrador J M, Larose S L and Sorond F A 2011 Dynamic cerebral autoregulation after intracerebral hemorrhage: a case-control study *BMC Neurol.* **11** 1–8

Pozrikidis C and Farrow D 2003 A model of fluid flow in solid tumors *Ann. Biomed. Eng.* **31** 181–94

Pries A R and Secomb T W 2005 Microvascular blood viscosity *in vivo* and the endothelial surface layer *Am. J. Physiol. Heart Circ. Physiol.* **289** H2657–64

Safaeian N and David T 2013 A computational model of oxygen transport in the cerebrocapillary levels for normal and pathologic brain function *J. Cereb. Blood Flow Metab.* **33** 1633–41

Schmid F, Barrett M J, Jenny P and Weber B 2019 Vascular density and distribution in neocortex *Neuroimage* **197** 792–805

Schmid F, Tsai P S, Kleinfeld D, Jenny P and Weber B 2017 Depth-dependent flow and pressure characteristics in cortical microvascular networks *PLoS Comput. Biol.* **13** e1005392

Secomb T, Hsu R, Beamer N and Coull B 2000 Theoretical simulation of oxygen transport to brain by networks of microvessels: effects of oxygen supply and demand on tissue hypoxia *Microcirculation* **7** 237–47

Seki H, Yoshimoto T, Ogawa A and Suzuki J 1985 Hemodynamics in hemorrhagic infarction–an experimental study *Stroke* **16** 647–51

Snarska K, Kapica-Topczewska K, Bachórzewska-Gajewska H and Małyszko J 2016 Renal function predicts outcomes in patients with ischaemic stroke and haemorrhagic stroke *Kidney Blood Press. Res.* **41** 424–33

Strandgaard S, Olesen J, Skinhøj E and Lassen N 1973 Autoregulation of brain circulation in severe arterial hypertension *BMJ* **1** 507–10
Stromberg D D and Fox J R 1972 Pressures in the pial arterial microcirculation of the cat during changes in systemic arterial blood pressure *Circ. Res.* **31** 229–39
Su S W, Catherall M and Payne S 2012 The influence of network structure on the transport of blood in the human cerebral microvasculature *Microcirculation* **19** 175–87
Tamaki K and Heistad D D 1986 Response of cerebral arteries to sympathetic stimulation during acute hypertension *Hypertension* **8** 911–7
Tan S, Wang D, Liu M, Zhang S, Wu B and Liu B 2014 Frequency and predictors of spontaneous hemorrhagic transformation in ischemic stroke and its association with prognosis *J. Neurol.* **261** 905–12
Terruso V, D'amelio M, Di Benedetto N, Lupo I, Saia V, Famoso G, Mazzola M A, Aridon P, Sarno C and Ragonese P 2009 Frequency and determinants for hemorrhagic transformation of cerebral infarction *Neuroepidemiology* **33** 261–5
Terzaghi K 1943 *Theor. Soil Mech.* (New York, NY: Wiley) pp 11–5
Thevathasan A, Naylor J, Churilov L, Mitchell P J, Dowling R J, Yan B and Kwan P 2018 Association between hemorrhagic transformation after endovascular therapy and poststroke seizures *Epilepsia* **59** 403–9
Tully B and Ventikos Y 2011 Cerebral water transport using multiple-network poroelastic theory: application to normal pressure hydrocephalus *J. Fluid Mech.* **667** 188–215
Van Kranendonk K R, Treurniet K M, Boers A M, Berkhemer O A, Coutinho J M, Lingsma H F, Van Zwam W H, Van Der Lugt A, Van Oostenbrugge R J and Dippel D W 2020 Added prognostic value of hemorrhagic transformation quantification in patients with acute ischemic stroke *Front. Neurol.* **11** 1335
Van Kranendonk K R, Treurniet K M, Boers A M, Berkhemer O A, Van Den Berg L A, Chalos V, Lingsma H F, Van Zwam W H, Van Der Lugt A and Van Oostenbrugge R J 2019 Hemorrhagic transformation is associated with poor functional outcome in patients with acute ischemic stroke due to a large vessel occlusion *J. Neurointerventional Surg.* **11** 464–8
Von Kummer R, Broderick J P, Campbell B C, Demchuk A, Goyal M, Hill M D, Treurniet K M, Majoie C B, Marquering H A and Mazya M V 2015 The Heidelberg bleeding classification: classification of bleeding events after ischemic stroke and reperfusion therapy *Stroke* **46** 2981–6
Wang J and Payne S J 2021 Mathematical modelling of haemorrhagic transformation after ischaemic stroke *J. Theor. Biol.* **531** 110920
Zweifach B W and Lipowsky H H 1977 Quantitative studies of microcirculatory structure and function. III. Microvascular hemodynamics of cat mesentery and rabbit omentum *Circ. Res.* **41** 380–90